Ni/CeO₂ Nanocatalysts with Optimized CeO₂ Support Morphologies for CH₄ Oxidation

Junjie Chen^{a,e}, Hien Pham^b, Tala Mon^a, Todd J. Toops^c, Abhaya K. Datye^b, Zhenglong Li^d, Eleni A. Kyriakidou^{a,*}

Notice: This manuscript has been co-authored by UT-Battelle, LLC, under Contract No. DE-AC0500OR22725 with the U.S. Department of Energy. The United States Government and the publisher, by accepting the article for publication, acknowledge that the United States Government retains a non-exclusive, paid-up, irrevocable, world-wide license to publish or reproduce the published form of this manuscript, or allow others to do so, for the United States Government purposes. The Department of Energy will provide public access to these results of federally accordance with DOE Public Plan sponsored research in the Access (http://energy.gov/downloads/doe-public-access-plan).

^a Department of Chemical and Biological Engineering, University at Buffalo, The State University of New York, Buffalo, NY 14260, USA

^b Department of Chemical and Biological Engineering and Center for Micro-Engineered Materials, University of New Mexico, Albuquerque, NM 87131, USA

^c Energy and Transportation Sciences Division, Oak Ridge National Laboratory, Oak Ridge, TN 37831, USA

^d Manufacturing Science Division, Oak Ridge National Laboratory, Oak Ridge, TN 37831, USA

^e Current address: SUNCAT Center for Interface Science and Catalysis, Department of Chemical Engineering, Stanford University, Stanford, CA 94305, USA

^{*} Corresponding author at: elenikyr@buffalo.edu (E.A. Kyriakidou).

Abstract

Catalytic oxidation of CH₄ over non-precious Ni/CeO₂ catalysts has attracted wide attention. Controlling the morphology of CeO₂ support can enhance the CH₄ oxidation activity without changing the catalyst composition. Herein, a series of 2 wt.% Ni/CeO₂ nanocatalysts with different CeO₂ support morphologies (nanoparticles (P), rods (R), cubes (C)) and synthetic procedures (precipitation, sol-gel) were evaluated for their CH₄ oxidation performance. The redox properties of CeO₂ supports and corresponding Ni loaded catalysts were characterized by H₂-temperature programmed reduction and oxygen storage capacity (OSC) measurements. The relationship between the CeO₂ morphologies, surface areas, redox properties, and CH₄ oxidation activity for both CeO₂ supports and Ni/CeO₂ catalysts was established. The findings suggest that CeO₂-R has a greater amount of surface oxygen vacancies, an improved OSC and CH₄ oxidation activity compared to CeO₂-P and CeO₂-C supports. The same CH₄ oxidation activity pattern was observed for the Ni containing catalysts (Ni/CeO₂-R > Ni/CeO₂-P > Ni/CeO₂-C). Increasing the CeO₂ surface area by using a sol-gel synthesis method (CeO₂-SG) improved the amount of surface oxygen vacancies and CH₄ oxidation performance of CeO₂-SG and Ni/CeO₂-SG compared to CeO₂-R and Ni/CeO₂-R, respectively. Finally, all studied Ni/CeO₂ nanocatalysts showed improved hydrothermal stability compared to conventional Pd/Al₂O₃.

Keywords: Ni/CeO₂, methane oxidation, morphology control, redox properties, support effect

1. Introduction

Ceria (CeO₂) has been widely investigated both as a catalyst and a catalyst support for a variety of catalytic reactions (i.e. catalytic oxidation of CO and hydrocarbons, 1-5 propane dehydrogenation,⁶ CH₄ reforming,⁷ water-gas shift reactions,⁸ nitric oxides reduction,⁹ etc.) attributed to its unique Ce⁴⁺/Ce³⁺ redox couple. ¹⁰ The morphology and surface properties of CeO₂ can play an important role on its catalytic performance. 11-15 Specifically, CeO₂ crystal planes can affect the oxygen vacancy concentration and impact the interaction of CeO2 with surface molecules.¹⁴ Recent advances in CeO₂ morphology control techniques provide a new approach to tailor the catalytic properties of CeO₂ by modifying the exposed facets. 11,16 Specifically, CeO₂ with different morphologies (nanoparticles, rods, cubes, octahedrons, nanoflowers) were synthesized and their catalytic performance towards different reactions was evaluated. For example, Ren et al.¹⁷ showed that the phenol oxidation performance of CeO₂ improves with increasing the surface oxygen defect concentration and Oads/Olatt ratio. Specifically, CeO2-filiform showed the highest surface oxygen defect concentration and improved activity compared to CeO₂cube, CeO₂-rod, and CeO₂-octahedron. Feng et al. 18 investigated the toluene oxidation performance of CeO2 with different morphologies (rod, hollow sphere, and cube) and the CeO2hollow spheres outperformed all studied samples (90% toluene conversion at 207 °C). The enhanced toluene oxidation performance of CeO₂-hollow spheres was attributed to their high surface area (130.2 m²/g) and abundant surface oxygen vacancies (Ce³⁺/(Ce³⁺+Ce⁴⁺)).

The morphology of CeO₂ plays an important role in the activity of metal supported CeO₂ catalysts, such as Ni/CeO₂, ¹⁹ Ru/CeO₂, ²⁰ Pt/CeO₂, ²¹ and Au/CeO₂. ¹⁹⁻²² Zhang et al. ¹⁹ reported that Ni/CeO₂-rod showed an improved propane oxidation performance compared to Ni/CeO₂-cube catalysts, attributed to the increased amount of strongly activated oxygen species of Ni/CeO₂-rods. On the other hand, Ni/CeO₂-cube had a greater amount of weakly activated oxygen species compared to Ni/CeO₂-rod catalysts resulting in an improved performance towards the oxidative dehydrogenation of propane reaction. The propane oxidation activity of Ru/CeO₂ (rod, cube, octahedra) was also investigated. ²⁰ The results indicated that the morphology of CeO₂ support can affect both the chemical state of Ru and the interaction between Ru-CeO₂. Ru/CeO₂-rods with CeO₂ (110) as the dominant facet showed an improved activity and stability towards the propane oxidation reaction.

Catalytic oxidation of methane (CH₄) to less harmful carbon dioxide (CO₂) is an efficient way for CH₄ emission control and has attracted significant attention.^{2, 23-25} Non-precious metal Ni/CeO₂-based catalysts have a promising CH₄ oxidation performance and they are more water resistant compared to platinum group metal (PGM)-based catalysts towards the CH₄ oxidation reaction.^{26,27} Our recent work showed that the CH₄ oxidation reaction over Ni/CeO₂ catalysts follows a Mars-van Krevelen mechanism, where the first C-H bond of CH₄ is cleaved at the Ni-CeO₂ interfacial site.²⁸ The reactivity of interfacial oxygen between Ni and CeO₂ can be tuned by tuning the exposed facets of CeO₂ supports. Therefore, controlling the exposed CeO₂ facets by adjusting the morphology of CeO₂ can potentially affect the Ni-CeO₂ interaction and the CH₄ oxidation activity of Ni/CeO₂ catalysts.

The impact of CeO₂ morphologies was studied over several reactions, including toluene oxidation¹⁸, propane oxidation and dehydrogenation of propane.¹⁹ Moreover, Ni/CeO₂ catalysts were utilized for the CH₄ oxidation reaction;^{27,28} however, the effect of the CeO₂ support morphologies on the redox properties and CH₄ oxidation performance of Ni/CeO₂ catalysts still remains unclear. In this work, the CH₄ oxidation performance of Ni supported on commercial CeO₂ and CeO₂ supports with different morphologies (nanoparticle, rod, cube) and synthesis methods (precipitation, sol-gel) is compared. The CH₄ oxidation performance of CeO₂ supports is also compared. The relationship between CeO₂ morphologies and the corresponding CH₄ oxidation activity of CeO₂ supports and Ni/CeO₂ catalysts was established though a combination of detailed characterizations including surface properties (Brunauer-Emmett-Teller (BET) surface area, Barrett-Joyner-Halenda (BJH) pore volume), redox properties (H₂-temperature programmed reduction (H₂-TPR), oxygen storage capacity (OSC)), CH₄ oxidation reaction rates and apparent activation energies. Finally, the CH₄ oxidation stability and H₂O resistance of Ni/CeO₂ catalysts was evaluated and compared to those of Pd/Al₂O₃ catalysts.

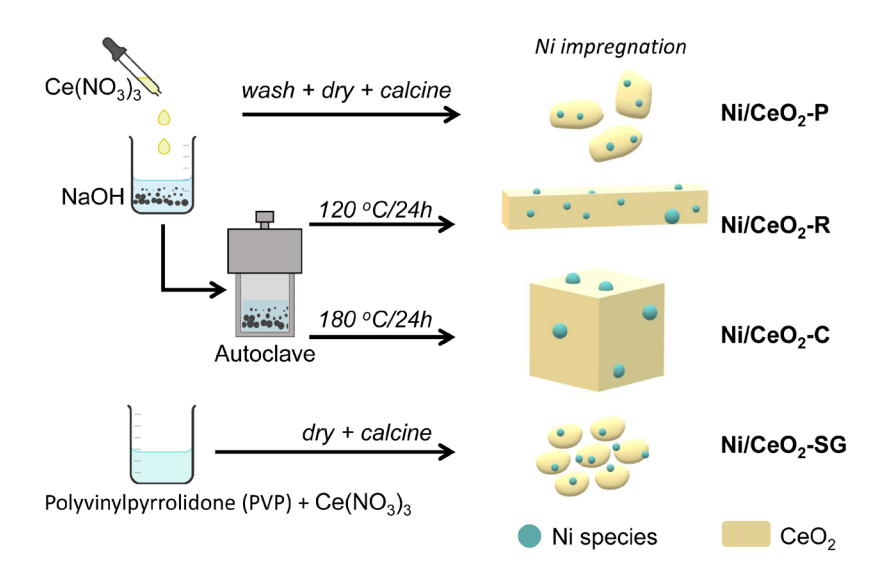
2. Experimental

2.1. Catalyst synthesis

CeO₂ supports with different morphologies (nanoparticles (P), rods (R), cubes (C)) were synthesized by precipitating Ce(NO₃)₃•6H₂O (99% purity (Sigma-Aldrich)) precursor solution in NaOH (ACS AR, Macron Fine Chemicals) solution, followed by hydrothermal synthesis at different temperatures (Scheme 1).^{20,29} Specifically, 1.74 g Ce(NO₃)₃•6H₂O and 19.2 g NaOH

were first dissolved in 10 and 70 mL D.I. water, respectively. The Ce(NO₃)₃•6H₂O solution was added drop-wisely in the NaOH solution. The final Ce-based suspension was stirred for 30 min at room temperature. CeO₂-P was synthesized by collecting the precipitant by centrifugation and washing it with D.I. water until the pH of the filtrate was close to neutral. CeO₂-R and CeO₂-C were synthesized by hydrothermal synthesis using the Ce-based suspension as precursor. Specifically, the Ce-based suspension was transferred into a 100 mL Teflon liner that was sealed in a stainless-steel autoclave followed by hydrothermal synthesis at 120 °C (CeO₂-R) or 180 °C (CeO₂-C) for 24 h. After the completion of the hydrothermal synthesis, the precipitate was collected and washed with D.I. water until the pH of the filtrate was close to 7. The synthesized CeO₂-P, CeO₂-R, and CeO₂-C supports were dried overnight at 110 °C, followed by calcination at 450 °C/5h (5 °C/min). CeO₂ was also synthesized with a polyvinylpyrrolidone (PVP)-assisted solgel method (CeO₂-SG).³⁰ Initially, 5 g of polyvinylpyrrolidone (PVP, average molecular weight 10,000 (Sigma-Aldrich)) was dissolved in 100 mL D.I. water followed by addition of 3.1 g of Ce(NO₃)₃•6H₂O. The solution was stirred for 1 h until a homogeneous and clear solution was obtained. The final solution was evaporated in a drying oven set at 110 °C. The resulting gel was calcined at 500 °C for 2h (10 °C/min). Commercial CeO2 (REacton, 99.9% purity), denoted as CeO₂-Com, from Alfa Aesar was also used for comparison purposes.

After the CeO₂ (P, R, C, SG, Com) supports were obtained, 2 wt.% Ni/CeO₂-P, R, C, SG, Com catalysts were synthesized by a wet impregnation method using Ni(NO₃)₂•6H₂O (99.9+% purity (Strem chemicals)) as a precursor. The Ni/CeO₂ catalysts were dried at 110 °C overnight, followed by calcination at 450 °C/5h (10 °C/min). 0.5 wt.% Pd/Al₂O₃ catalyst was also synthesized for comparison purposes by incipient wetness impregnation using Pd(NO₃)₂•4 NH₃ solution (10 wt.% in H₂O (Sigma Aldrich)) and γ-Al₂O₃ (Sasol) as reported previously.²⁷



Scheme 1. Synthesis of Ni/CeO₂-P, R, C by precipitation, hydrothermal, and polyvinylpyrrolidone (PVP)-assisted sol-gel synthesis.

2.2. Characterization

The BET surface areas and BJH pore volumes of CeO₂-P, R, C, SG, Com supports were measured by N₂ adsorption and desorption experiments using a Tri-Star II surface area and porosity analyzer (Micromeritics). The samples were degassed at 150 °C for 3 h (Micromeritics VacPrep 061) prior to surface area and pore volume measurements. The BJH pore volumes were obtained from the desorption branch of the collected isotherms.

The crystalline structure of CeO₂-P, R, C, SG, Com supports was determined by X-ray diffraction (XRD) and their crystal size was calculated using the Scherrer equation.³¹ The XRD patterns of all studied CeO₂ supports were collected with a Rigaku Ultima IV equipment (Cu K α X-ray source) from $2\theta = 5$ to 90° with a step size of 1.0167° and scan speed of 2° /min.

The exposed facets of CeO₂-P, R, C, SG supports were determined by obtaining high resolution transmission electron microscopy (HRTEM) images that were collected with a JEOL JEM 2020 instrument. The CeO₂ supports were dusted on Cu grids and they were purged with compressed air to remove excess powder. Additional HRTEM of Ni loaded catalysts were collected with a JEOL NEOARM 200CF transmission electron microscope equipped with spherical aberration correction to allow atomic resolution imaging, and an Oxford Aztec Energy Dispersive System (EDS) for elemental analysis. The microscope is equipped with two large area JEOL EDS detectors for higher throughput in acquisition of x-ray fluorescence signals. Images

were recorded in annular dark field (ADF) mode and in annular bright field (ABF) mode, and in HRTEM mode.

Ni loading over Ni/CeO₂ catalysts was determined by inductively coupled plasma optical emission spectrometer (ICP-OES, Thermo Scientific iCAP 6000). Prior to the ICP analysis, about 20 mg of each catalyst was digested in 20 mL HNO₃ (63 wt.%) at 80 °C for 24 h.

Raman spectra of CeO₂-P, R, C, SG, Com supports were obtained with a Renishaw inVia Raman microscope. Excitation wavelength of 514 nm was used for all data collection.

O₂, CO pulse chemisorption and H₂-TPR were conducted on AutoChem II 2920 (Micromeritics). The OSCs of CeO₂-P, R, C, SG, Com supports were determined by O₂ pulse chemisorption as reported previously.²⁷ Briefly, 50 mg of sample was first reduced at 450 °C for 1 h with 10% H₂/Ar, followed by 30 mins Ar purging at the same temperature to remove gas phase H₂. A series of O₂ pulses were then injected to the sample until the sample was saturated. The O₂ uptake calculated based on the first pulse was used to determine the sample OSC. The oxygen storage capacity complete (OSCC) was calculated based on the cumulative O₂ uptake.

The reducibility of CeO₂-P, R, C, SG, Com supports, and Ni loaded catalysts (Ni/CeO₂-P, R, C, SG, Com) was determined by H₂-TPR. Specifically, 50 mg of sample was loaded in a U-shaped quartz tube reactor and it was initially oxidized (20% O₂/Ar, 50 sccm (cm³ min⁻¹ (STP)) at 400 °C for 30 min (10 °C/min)) followed by cooling down to room temperature under pure Ar (Ultra high purity, Airgas). The feed gas was then switched to 10% H₂/Ar. Once the thermal conductivity detector (TCD) signal was stabilized, the sample was heated up to 1005 °C with a temperature ramp of 10 °C/min. The H₂ consumption was recorded by the TCD.

2.3. Catalytic performance evaluation

The CH₄ oxidation performance of CeO₂-P, R, C, SG, Com supports and Ni/CeO₂-P, R, C, SG, Com catalysts was evaluated in a home-built packed bed reactor equipped with an online MKS FTIR gas analyzer (MultiGas 2030).³² For each test, 100 mg of sample diluted with 100 mg quartz sand was loaded in a U-shaped quartz tube reactor (I.D. = 8 mm) and was stabilized between two small plugs of quartz wool. The feed gas contained CH₄: O₂: Ar = 1:5:9 and it was well mixed before introduced in the reactor. The total flow of the feed gas was 30 sccm (gas hourly space velocity (GHSV) ~ 18,000 mLg⁻¹h⁻¹). The CH₄ oxidation light-off curves were collected while heating the samples from 200 to 750 °C (10 °C/min). Three consecutive light-off curves were

collected for each sample to determine its stability. The effluent gas was diluted 10 times with Ar to minimize the response time of the gas analyzer. CH_4 conversions (X) were calculated using Eq. (1).

CH₄ conversion:
$$X = \frac{(c_{\text{CH}_4,\text{in}} - c_{\text{CH}_4,\text{out}})}{c_{\text{CH}_4,\text{in}}} \times 100\%$$
 (Eq. 1)

where $C_{\text{CH}_4,\text{in}}$ and $C_{\text{CH}_4,\text{out}}$ are the CH₄ concentrations in the inlet and outlet of the reactor, respectively.

The CH₄ oxidation rates of CeO₂-P, R, C, SG, Com supports and Ni/CeO₂-P, R, C, SG, Com catalysts were measured at steady state. The catalysts were kept at each reaction temperature for at least 1 h. The reaction rates were measured at $X_{\text{CH}_4} < 15\%$ to minimize heat and mass transfer effects. The apparent activation energies (E_{app}) of CeO₂-P, R, C, SG, Com supports and Ni/CeO₂-P, R, C, SG, Com catalysts were calculated from the Arrhenius plot. CH₄ oxidation rates (r) were calculated using Eqs. (2-3).

Reaction rate:
$$r(\mu \text{mol}_{\text{CH}_4} \text{g}_{\text{cat}}^{-1} \text{s}^{-1}) = \frac{c_{\text{CH}_4,\text{in}} \left(30 \times \frac{10^{-3} \text{L}}{60 \text{ s}}\right) \times 10^{6} \frac{\mu \text{mol}}{\text{mol}}}{22.4 \frac{\text{L}}{\text{mol}} \times 0.1 \text{g}_{\text{cat}}} \times X$$
 (Eq. 2)

Reaction rate:
$$r(\mu \text{mol}_{\text{CH}_4} g_{\text{Ni}}^{-1} s^{-1}) = \frac{C_{\text{CH}_4,\text{in}} \left(30 \times \frac{10^{-3} \text{L}}{60 \text{ s}}\right) \times 10^{6} \frac{\mu \text{mol}}{\text{mol}}}{22.4 \frac{\text{L}}{\text{mol}} \times 0.1 g_{\text{cat}} \times M_{\text{Ni}}} \times X$$
 (Eq. 3)

where M_{Ni} is the Ni loading (2 wt.%).

The stability of Ni/CeO₂-P, R, C, SG, Com and 0.5 wt.% Pd/ γ -Al₂O₃ catalysts in the presence of water was evaluated by initially keeping the catalyst inlet temperature at 450 °C for 12 h under the following conditions: CH₄: O₂: Ar = 1 : 5 : 9 (GHSV ~ 18,000 mLg⁻¹h⁻¹). Subsequently, 5% H₂O was introduced in the reactor for 12 h to evaluate the hydrothermal stability of the studied catalysts. A syringe pump (D-series pump (Teledyne Isco)) was used to supply water in a tube furnace (200 °C) where water was instantly vaporized and carried to the reactor by Ar. Finally, the water was removed from the feed gas mixture and the recoverability of the studied catalysts was evaluated over a 10 h period.

3. Results and discussions

3.1. Textural properties of CeO₂-P, R, C, SG, Com supports

The N_2 adsorption/desorption isotherms of CeO₂-P, R, C, SG, Com supports are shown in Fig. S1. The support surface areas decrease in the following order: CeO₂-SG (125 m²/g) > CeO₂-

P (96 m²/g) > CeO₂-R (75 m²/g) > CeO₂-C (19 m²/g) > CeO₂-Com (0.8 m²/g) (Table 1). CeO₂-R, C had a lower surface area compared to CeO₂-P due to the growth of the crystal size of CeO₂ during hydrothermal synthesis (see XRD data discussion). However, the pore volume increased from $0.12 \text{ cm}^3/\text{g}$ (CeO₂-P) to $0.18 \text{ cm}^3/\text{g}$ (CeO₂-C) to $0.47 \text{ cm}^3/\text{g}$ (CeO₂-R), which can be attributed to the increased void between nanocrystals in CeO₂-R, C supports. The surface area and crystallite size of CeO₂-SG is consistent with literature results for CeO₂-SG synthesized by similar methods.³⁰ The higher surface area of CeO₂-SG but larger crystallite size than CeO₂-P is likely due to improved porosity of CeO₂-SG (0.22 cm³/g) than CeO₂-P (0.12 cm³/g) and the defective nature of the crystals, grain boundaries.

Table 1. BET surface areas (SA), BJH pore volumes (PV), average crystallite size, OSC and OSCC of the CeO₂-P, R, C, SG, Com supports.

Sample	SA (m ² /g)	PV (cm ³ /g)	Average crystallite size (nm) ^a	OSC (µmol/g)	OSCC (µmol/g)
CeO ₂ -P	96	0.12	5.2	107	108
CeO ₂ -R	75	0.47	9.4	125	126
CeO ₂ -C	19	0.18	33.9	44	48
CeO ₂ -SG	125	0.22	7.7	158	161
CeO ₂ -Com	0.8	0.003	45.6	3	5

^a average crystallite sizes were calculated from XRD patterns using the Scherrer equation (peaks: 111, 200, 220, 311).

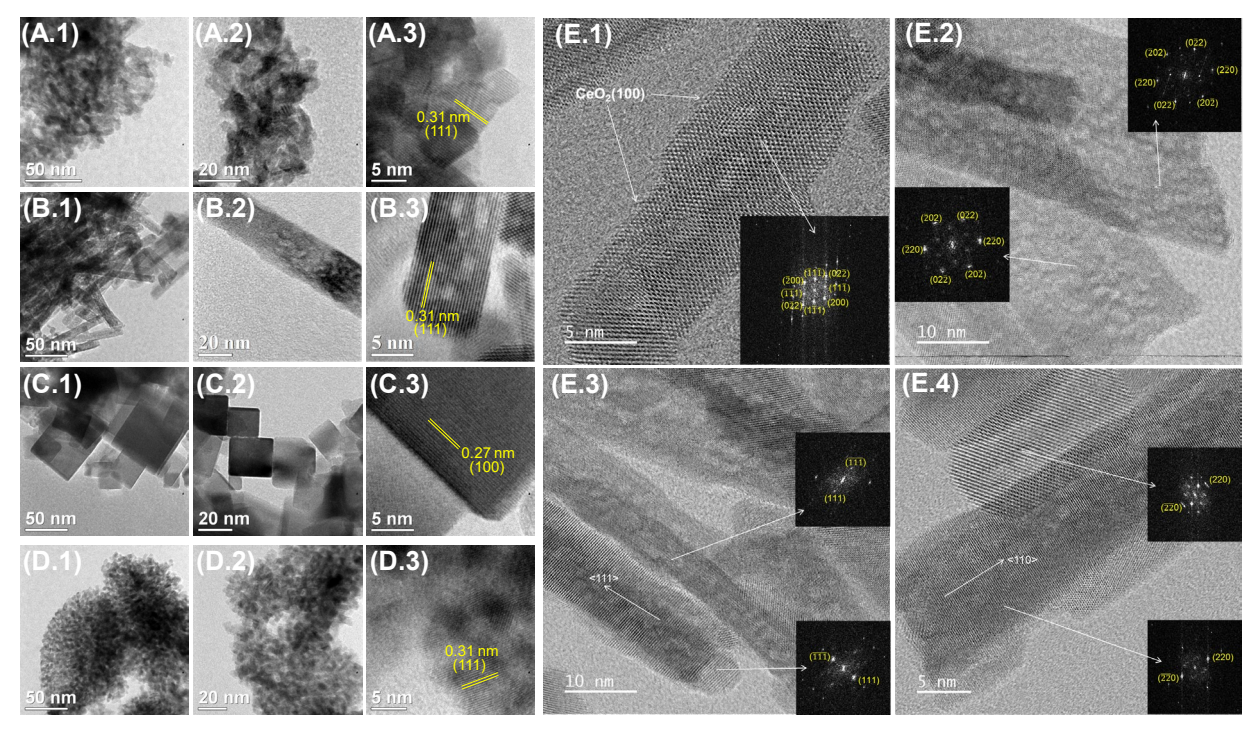


Fig. 1. HRTEM images of A.(1-3) CeO₂-P, B.(1-3) CeO₂-R, C.(1-3) CeO₂-C, and D.(1-3) CeO₂-SG. (E.1-4) ABF-STEM images of the ceria rods in Ni/CeO₂-R after stability test, and their FFT patterns. The diffraction spots in the FFT patterns are indexed to show the planes corresponding to the lattice fringes of CeO₂.

HRTEM images (Fig. 1) of the CeO₂-P, R, C, SG supports confirm their unique morphologies. CeO₂-P synthesized by precipitation of the Ce precursor in an alkaline solution is present as nanocrystals. Hydrothermal synthesis at 120 °C led to the formation of rod-shaped CeO₂ (Fig. 1(B.1-3)), as was described previously.²⁰ Fig. 1(E.1-4) shows ABF-STEM images of CeO₂ rods and their FFT patterns in Ni/CeO₂-R catalyst. The diffraction spots in the FFT patterns were indexed to show the planes corresponding to the lattice fringes of CeO₂. The FFT patterns shown in Fig. 1(E.1) and Fig. 1(E.2) indicate that the images are oriented in the [110] and [111] zone axes, respectively. CeO₂ rod has exposed well-faceted (100) surfaces (Fig. 1(E.1)). However, many of the CeO₂ rods have undulating surfaces (Fig. 1(E.2-4)), and therefore, these surfaces cannot be assigned to a specific facet. In Fig. 1(E.3), ceria rods appear to expose a (111) surface and the rods appear to grow in the <111> and <110> directions (Fig. 1(E.4)), as indexed in the FFT patterns. This characterization is consistent with previous work showing that the dominant facet shown on ceria nanorods is most likely (111), and catalytic data was confirmed by AC-STEM and water-gas shift reactivity.³³ Hydrothermal synthesis at 180 °C generated cube-shaped CeO₂ with (100) as

the main surface facet (Fig. 1(C.1-3)).⁴ High surface area CeO₂ synthesized by sol-gel method resulted to uniform CeO₂ nanocrystals (Fig. 1(D.1-3)) with (111) surface exposed.

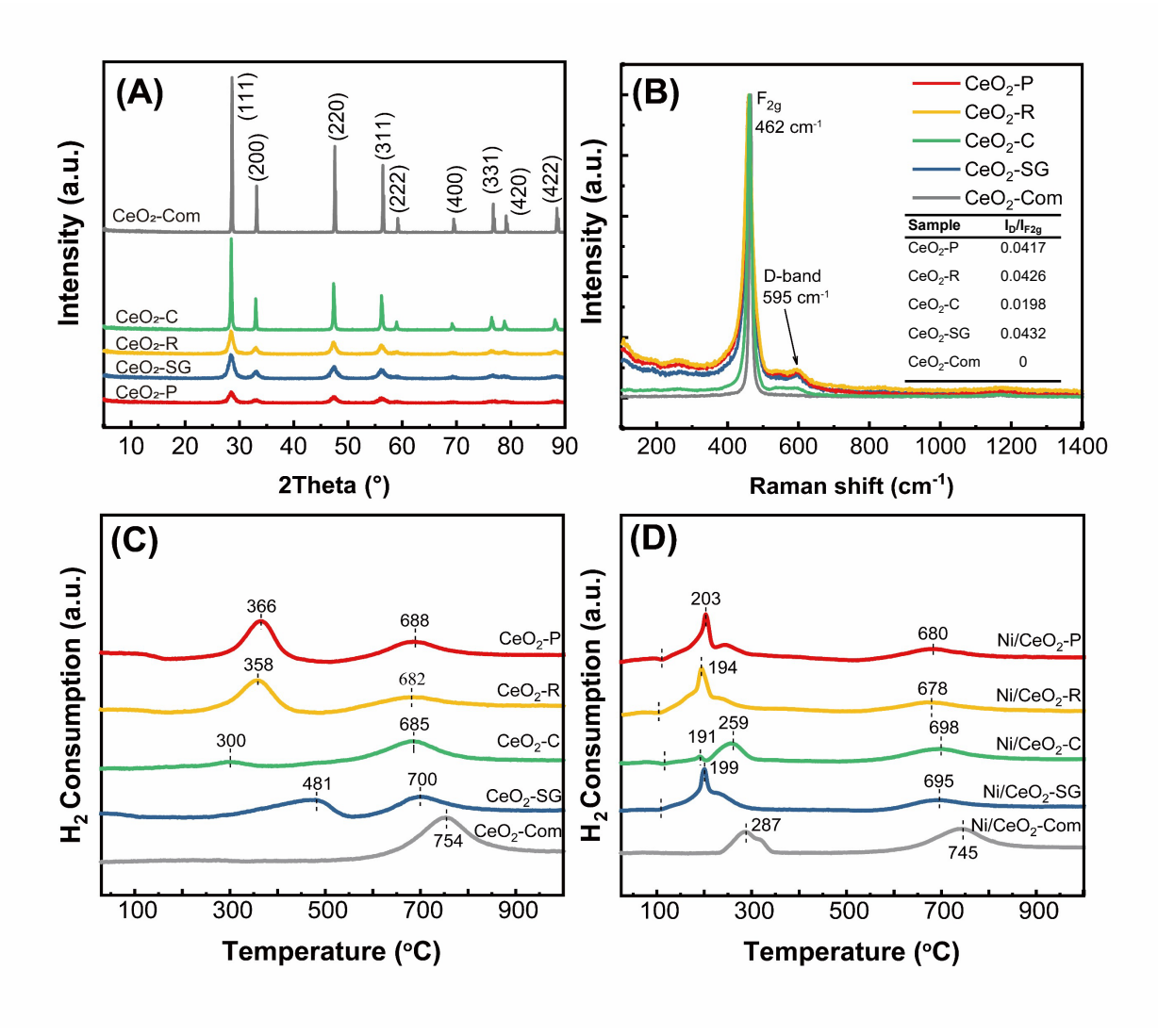


Fig. 2. (A) XRD patterns, (B) Raman spectra and I_D/I_{F2g} ratios, (C) H_2 -TPR profiles of CeO₂-P, R, C, SG, Com supports, and (D) H_2 -TPR profiles of Ni/CeO₂-P, R, C, SG, Com catalysts.

All CeO₂ supports showed an identical cubic fluorite phase (JCPDS 34-0394) (Fig. 2(A)). The XRD peaks at 28.3° , 32.8° , 47.0° , and 55.8° correspond to (111), (200), (220), and (311) facets, respectively. CeO₂-P had the smallest crystallite size (5.2 nm) of all studied CeO₂ supports (Table 1). Hydrothermal synthesis of CeO₂-R and CeO₂-C led to the growth of the crystallite size as follows: CeO₂-P (5.2 nm) < CeO₂-R (9.4 nm) < CeO₂-C (33.9 nm). This observation is consistent with the decrease in the surface area observed over the same samples (Table 1). CeO₂-

SG had a slightly larger crystallite size (7.7 nm) than CeO₂-P (5.2 nm) and CeO₂-Com had the largest crystalline size (45.6 nm) of all studied CeO₂ supports.

The redox properties of CeO₂-P, R, C, SG, Com supports were characterized by O₂ pulse chemisorption, Raman, and H₂-TPR. CeO₂-Com had the lowest O₂ uptake (3 μmol/g) compared to all studied CeO₂ supports, that is associated with its low surface area (0.8 m²/g) and well crystalized nature (crystallite size: 45.6 nm) (Table 1). CeO₂-R had a greater OSC (125 μmol/g) compared to CeO₂-P (107 μmol/g) even though CeO₂-R has a larger crystallite size and a smaller surface area compared to CeO₂-P. This suggests that the oxygen species over CeO₂ (110) facets present in CeO₂-R supports have higher reactivity compared to CeO₂ (111) facets present in CeO₂-P supports.¹⁹ However, CeO₂-C had a lower OSC/OSCC compared to CeO₂-P and CeO₂-R, which can be attributed to its lower surface area and lower reactivity of oxygen species on CeO₂ (100) facets. CeO₂-SG had the greatest OSC (158 μmol/g) and surface area of all studied supports, suggesting that increasing the surface area can increase the total amount of defect sites over the CeO₂ surface.

The surface redox properties of the studied CeO₂ supports were further characterized by Raman spectroscopy, as surface oxygen vacancies are highly sensitive to the D band intensity. The Raman spectra of CeO₂-P, R, C, SG, Com supports (Fig. 2(B)) contain two main peaks: F_{2g} at 462 cm⁻¹ and a defect-induced D-band at 595 cm⁻¹. The relative amount of surface oxygen vacancies can be compared by the ratio of the intensities of the D-band and F_{2g} peaks (I_D/I_{F2g}). The I_D/I_{F2g} ratio increases in the same order as the OSC of the CeO₂ support (SG > R > P > C > Com) (Table 1), suggesting that the observed increase in the OSC of CeO₂ supports can originate from the increase in surface oxygen vacancies. The Raman data further indicates that CeO₂-R has higher concentration of oxygen vacancies compared to CeO₂-P and CeO₂-C.

The H₂-TPR profiles of CeO₂-P, R, C, SG, Com supports are shown in Fig. 2(C). Two main H₂ consumption peaks centered at 366 and 688 °C are present over CeO₂-P, that can be attributed to the reduction of surface/sublayer and bulk phase Ce⁴⁺ to Ce³⁺, respectively.²⁷ The H₂ consumption profile of CeO₂-R is similar to the one of CeO₂-P with the surface Ce⁴⁺ reduction peak shifted to a slightly lower temperature (358 °C). The surface Ce⁴⁺ of CeO₂-C is reduced at a lower temperature (300 °C) compared to CeO₂-P (366 °C) and CeO₂-R (358 °C), which can be attributed to the decreased surface area of CeO₂-C compared to CeO₂-P, R resulting to a decreased amount of reducible surface oxygen. CeO₂-SG has a broad surface Ce⁴⁺ reduction peak centered

at 481 °C. No surface Ce⁴⁺ reduction peak was observed over CeO₂-Com attributed to its low surface area (0.8 m²/g) and large crystallite size (45.6 nm). Bulk Ce⁴⁺ present in CeO₂-P, R, C, SG, Com was reduced from 682-754 °C. Nickel incorporation in CeO₂-P, R, C, SG, Com supports promoted the reduction of surface/sublayer Ce⁴⁺ due to the interaction between Ni and CeO₂ (Fig. 2(D)).²⁷ Specifically, all surface/sublayer Ce⁴⁺ reduction peaks over Ni/CeO₂ catalysts shifted to lower temperatures compared to the surface/sublayer Ce⁴⁺ reduction peaks of their corresponding CeO₂ supports. On the contrary, bulk CeO₂ present in Ni/CeO₂ catalysts was reduced at a similar temperature compared to bulk CeO₂ in CeO₂ supports indicating the lack of interaction between surface Ni and bulk CeO₂. Reduction peaks starting at low temperatures (~100 °C) can be attributed to the reduction of adsorb oxygen species on the CeO₂ surface and interface oxygen between Ni and CeO₂.²⁷ The low temperature peaks ~ 200 °C over Ni/CeO₂ -P, R, SG are attributed to the reduction of Ni-O-Ce, while the shoulders observed at a slightly higher temperature are assigned to the reduction of surface CeO₂.²⁷ New H₂ consumption peaks at 259 and 287 °C appeared over Ni/CeO2-C and Ni/CeO2-Com, respectively, which are attributed to the reduction of large NiO particles.³⁶ The intensity of the interface oxygen reduction peaks over Ni/CeO₂-P, R, SG was greater than that of Ni/CeO₂-C, Com. This observation suggested the presence of a greater amount of interfacial oxygen species over Ni/CeO₂-P, R, SG than Ni/CeO₂-C, Com. Therefore, nickel dispersion is greater over high surface area CeO₂-P, R, SG than low surface area CeO₂-C, Com supports.

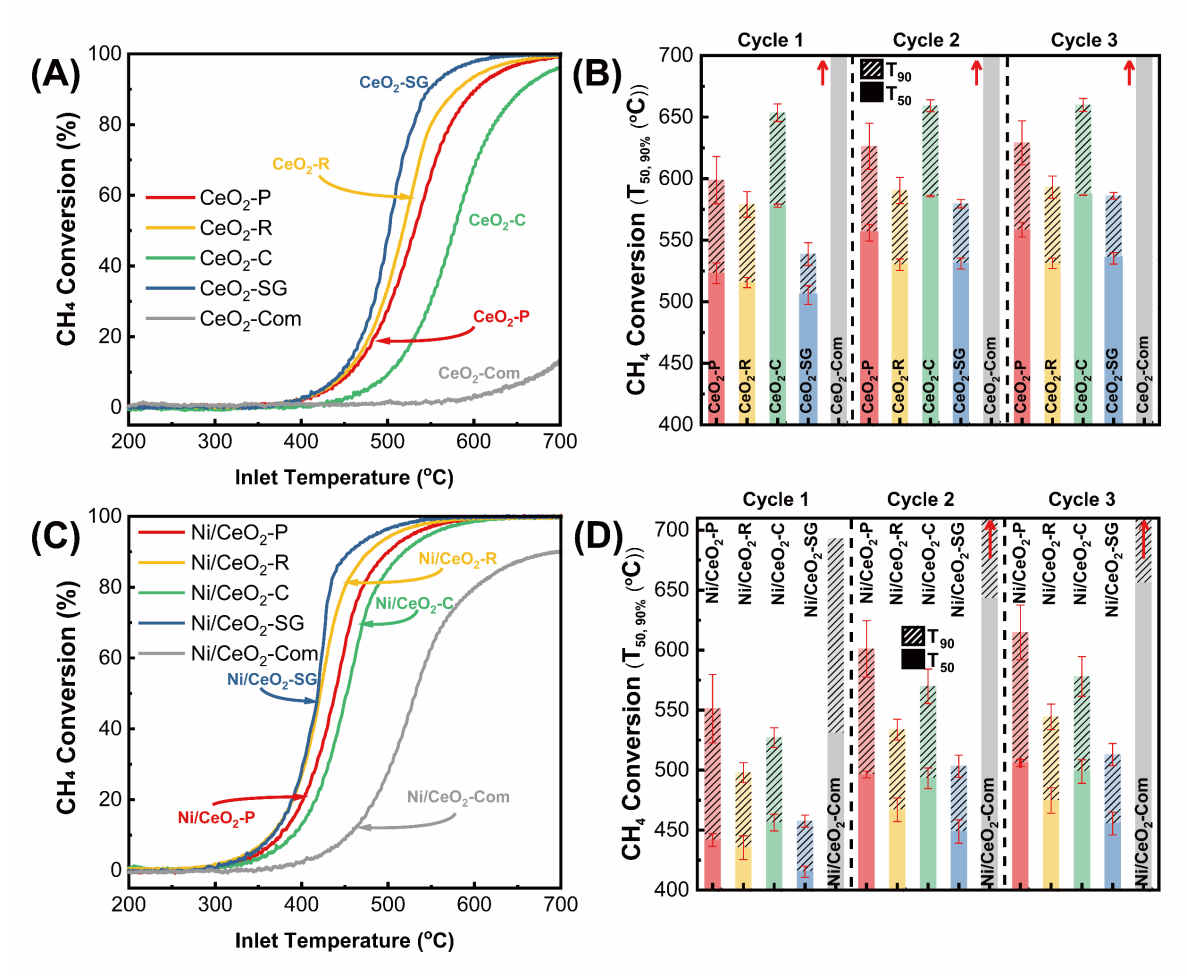


Fig. 3. (A) CH₄ oxidation light-off curves and (B) T_{50,90}'s of CH₄ conversion over three consecutive light-off cycles for CeO₂-P, R, C, SG, Com supports; (C) CH₄ oxidation light-off curves and (D) T_{50,90}'s of CH₄ conversion over three consecutive light-off cycles for Ni/CeO₂-P, R, C, SG, Com catalysts.

3.2. CH₄ oxidation performance

CeO₂-SG showed the best CH₄ oxidation performance followed by CeO₂-R, CeO₂-P, CeO₂-C, and CeO₂-Com (Fig. 3A). CeO₂-SG, CeO₂-R, and CeO₂-P reached 100% CH₄ conversion below 700 °C. However, CeO₂-C failed to reach 100% CH₄ conversion up to 700 °C, while only 12% of CH₄ was converted at 700 °C over CeO₂-Com. The temperatures that 50 and 90% CH₄ conversion was achieved (T₅₀ and T₉₀, respectively) over CeO₂-P, R, C, SG, Com supports in three consecutive light-off cycles are summarized in Fig. 3(B). CeO₂-R had lower T_{50,90}'s compared to CeO₂-P in all cycles suggesting that the oxygen species in CeO₂-R are more active than those in CeO₂-P towards the CH₄ oxidation reaction. The improved CH₄ oxidation performance of CeO₂-R compared to CeO₂-P can be also explained by the greater OSC (Table 1) and I_D/I_{F2g} ratio (Fig.

2(B)) of CeO₂-R compared to CeO₂-P. Increasing the hydrothermal synthesis temperature from 120 to 180 °C led to the transformation of CeO₂-P to CeO₂-C, resulting to an increase in the T₅₀ and T₉₀ from 523 and 599 °C to 578 and 654 °C, respectively. CeO₂-SG that had the highest surface area between all studied supports showed the lowest T_{50,90}'s, indicating that enhancing the CeO₂ surface area through a sol-gel synthesis can result to an improved CH₄ oxidation performance. The T_{50,90}'s of the studied CeO₂ supports were increased in the same order during the three consecutive light-off cycles (CeO₂-SG < CeO₂-R < CeO₂-P < CeO₂-C < CeO₂-Com) (Fig. 3(A, B), Fig. S2). However, there was a greater increase in Δ T₅₀ = 30 °C and Δ T₉₀ = 47 °C (Δ T_{50,90} = T_{50,90} (cycle 3) – T_{50,90} (cycle 1)) over CeO₂-SG , compared to CeO₂-R (Δ T₅₀ = 16 °C and Δ T₉₀ = 14 °C) and CeO₂-C (Δ T₅₀ = 9 °C and Δ T₉₀ = 6 °C). The decreased Δ T_{50,90} of CeO₂-R and CeO₂-C compared to CeO₂-SG can be attributed to the improved thermal stability of CeO₂-R that has a larger crystallite size.

Incorporation of Ni enhanced the CH₄ oxidation performance of CeO₂-P, R, C, SG, Com supports significantly (Fig. 3(C, D)). The enhanced CH₄ oxidation performance can be attributed to the interaction between Ni and CeO₂ supports that can improve the catalyst reducibility and interfacial oxygen reactivity.²⁷ Ni/CeO₂-P, R, C, SG can fully convert CH₄ at temperatures below 600 °C, whereas Ni/CeO₂-Com was not able to reach 100% CH₄ conversion at 700 °C. The CH₄ oxidation performance of Ni/CeO₂ catalysts and CeO₂ supports showed the same pattern, emphasizing that CeO₂ supports play a key role in the activity of Ni/CeO₂. Moreover, the T_{50,90}'s of Ni/CeO2 catalysts decreased with increasing the OSCs of the CeO2 supports, suggesting that more reactive oxygen from the CeO₂ supports can improve the CH₄ oxidation performance of Ni/CeO₂ catalysts. Fig. S3 shows three consecutive light-off cycles over the studied Ni/CeO₂ catalysts with their T_{50,90}'s summarized in Fig. 3(D). The CH₄ oxidation performance pattern was maintained over three consecutive light-off cycles (Ni/CeO₂-SG > Ni/CeO₂-R > Ni/CeO₂-P > Ni/CeO₂-C > Ni/CeO₂-Com). A more severe deactivation was observed over Ni/CeO₂ catalysts from cycle 1 to 2 compared to CeO₂ supports, that showed only a minor deactivation during cycling. The deactivation during cycling observed over the Ni/CeO₂ catalysts can be attributed to Ni sintering due to exposure to high temperatures (750 °C).

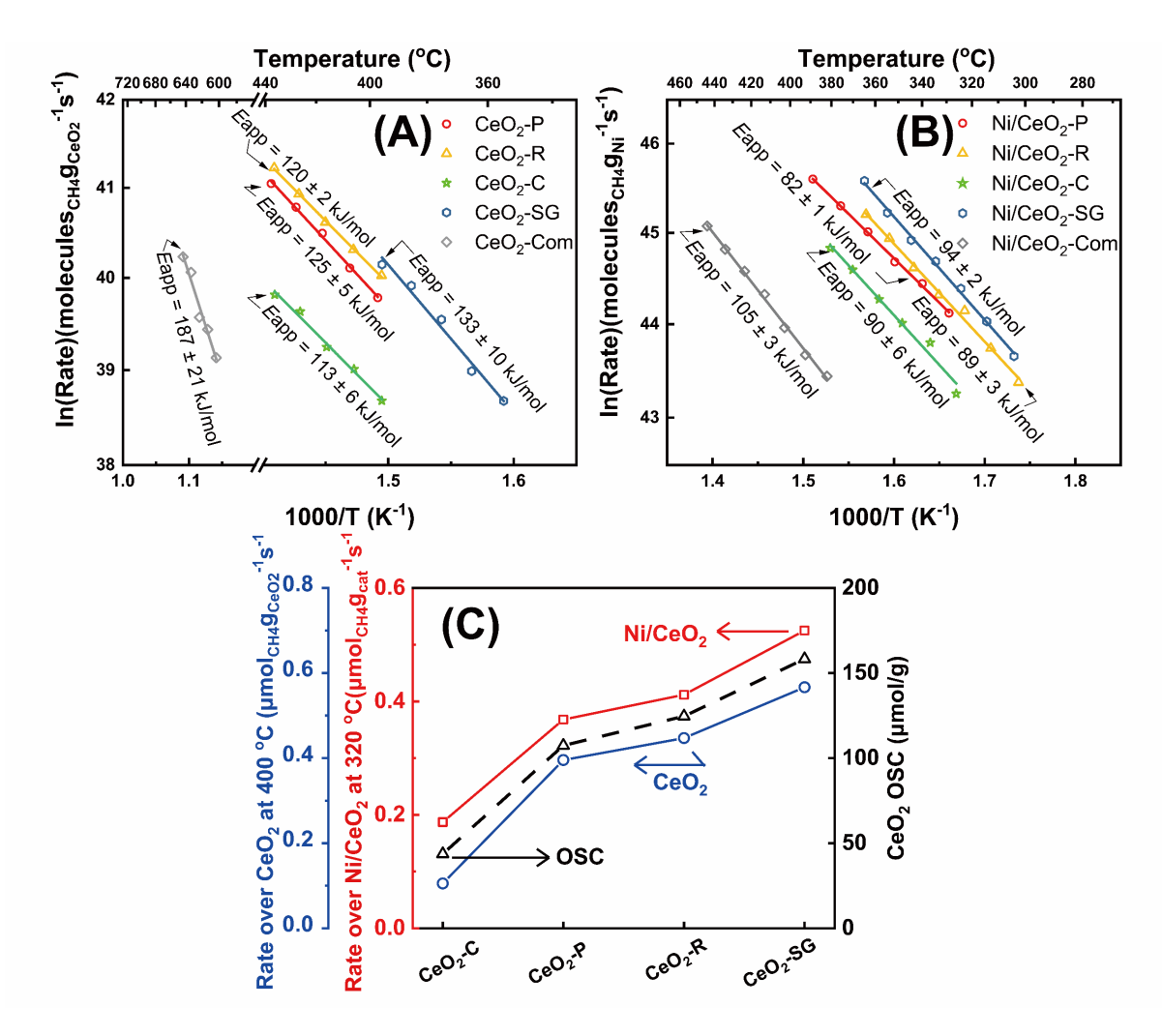


Fig. 4. Arrhenius plot and apparent activation energies of (A) CeO₂-P, R, C, SG, Com supports and (B) Ni/CeO₂-P, R, C, SG, Com catalysts. (C) CH₄ oxidation rates of CeO₂-P, R, C, SG supports at 400 °C and Ni/CeO₂-P, R, C, SG catalysts at 320 °C as a function of the OSC of the corresponding CeO₂ supports.

3.3. Apparent activation energies and reaction rates

The Arrhenius plots and apparent activation energies of CH₄ oxidation over CeO₂ supports and Ni/CeO₂ catalysts are shown in Fig. 4(A, B) and Table 2. The apparent activation energies of CeO₂-P, R, C, SG supports vary from 113-133 kJ/mol, with CeO₂-C having the lowest (113 kJ/mol) and CeO₂-SG the highest (133 kJ/mol) *E*app. The *E*app of CeO₂-Com (187 kJ/mol) was greater than that of all the other CeO₂-P, R, C, SG supports, which can be attributed to the gas phase oxidation of CH₄ at temperatures > 600 °C. ¹⁸ The *E*app's of Ni/CeO₂-P, R, C, SG, Com catalysts (82-105 kJ/mol) are lower than those of CeO₂-P, R, C, SG, Com supports and Ni/quartz sand (120 kJ/mol²⁷), suggesting a synergistic effect between Ni and CeO₂-P, R, C, SG, Com supports.

However, the Eapp of Ni/CeO₂-Com (105 ± 3 kJ/mol) is similar to the Eapp of Ni/quartz sand,²⁷ suggesting that Ni/CeO₂-Com has a limited number of interfacial Ni-O-Ce sites attributed to the low surface area of CeO₂-Com ($0.8 \text{ m}^2/\text{g}$).

Table 2. Apparent activation energies (*E*app) of CeO₂-P, R, C, SG, Com supports and Ni/CeO₂-P, R, C, SG, Com catalysts.

Sample	Eapp (kJ/mol)	Sample	Eapp (kJ/mol)
CeO ₂ -P	125 ± 5	Ni/CeO ₂ -P	82 ± 1
CeO ₂ -R	120 ± 2	Ni/CeO ₂ -R	89 ± 3
CeO ₂ -C	113 ± 6	Ni/CeO ₂ -C	90 ± 6
CeO ₂ -SG	133 ± 10	Ni/CeO ₂ -SG	94 ± 2
CeO ₂ -Com	187 ± 21	Ni/CeO ₂ -Com	105 ± 3

The relationship between the CH₄ oxidation reaction rate of CeO₂ supports and Ni/CeO₂ catalysts with the OSC of CeO₂ supports is shown in Fig. 4(C). Hydrothermal synthesis at 120 °C transformed CeO₂-P (dominating facet (111)) to CeO₂-R (dominating facet (110)) leading to an increase in the support OSC from 107 μmol/g (CeO₂-P) to 125 μmol/g (CeO₂-R) as well as the mass-specific CH₄ oxidation reaction rate. Hydrothermal synthesis at 180 °C generated CeO₂-C with decreased OSC (44 μmol/g) and lower CH₄ oxidation rate (0.105 μmol_{CH₄}g_{CeO₂}-1_s-1) at 400 °C compared to all studied CeO₂ supports. CeO₂-SG has the highest OSC and CH₄ oxidation rate compared to all studied supports. The same pattern between the OSC of CeO₂ and the CH₄ oxidation rate was maintained after incorporation of 2 wt.% Ni on CeO₂-P, R, C, SG.

3.4. CH₄ oxidation stability and H₂O resistance

The stability of Ni/CeO₂ catalysts under dry/wet feed is shown in Fig. 5. The stability of 0.5 wt.% Pd/Al₂O₃ was also evaluated for comparison. 0.5 wt.% Pd/Al₂O₃ had the highest initial CH₄ conversion ($X_{\text{CH}_4} = 90\%$) at 450 °C among the studied catalysts. However, a continuous

deactivation was observed over 0.5 wt.% Pd/Al₂O₃ within the first 12 h in the dry feed experiment, where the CH₄ conversion decreased from 90 to 58%. A possible explanation for the deactivation observed over 0.5 wt.% Pd/Al₂O₃ is that H₂O generated through CH₄ oxidation reaction (3.9-6%) can lead to OH group accumulation on Al₂O₃ and Pd.³⁷ The CH₄ conversion of Pd/Al₂O₃ was inhibited even further ($X_{\text{CH}_4} \sim 40\%$) when 5% H₂O was introduced in the reactor at time = 12 h. When 5% H₂O was removed from the feed gas (time = 24 h) the CH₄ conversion was recovered to the level before the introduction of H₂O, suggesting that the catalyst was stabilized when exposed to dry feed for 12 h. Ni/CeO₂ catalysts showed an improved CH₄ oxidation stability and only a minor deactivation compared to Pd/Al₂O₃. For example, in the first 12 h of the dry feed stability test, the CH₄ conversion of Ni/CeO₂-SG decreased only from 80 to 75%. Moreover, H₂O inhibition was reversible over all Ni/CeO₂ catalysts, where the CH₄ oxidation performance was fully recovered after H₂O was removed from the reactor feed. The CH₄ oxidation performance during the stability tests followed the same pattern as the light-off tests: Ni/CeO₂-SG > Ni/CeO₂-R > Ni/CeO₂-P > Ni/CeO₂-C > Ni/CeO₂-Com. The CH₄ conversion of Ni/CeO₂-P, R, SG catalysts at the end of the stability test was greater than that of Pd/Al₂O₃. This result highlights the potential of using Ni/CeO₂ as a non-PGM alternative to Pd/Al₂O₃ catalysts for the CH₄ oxidation reaction.

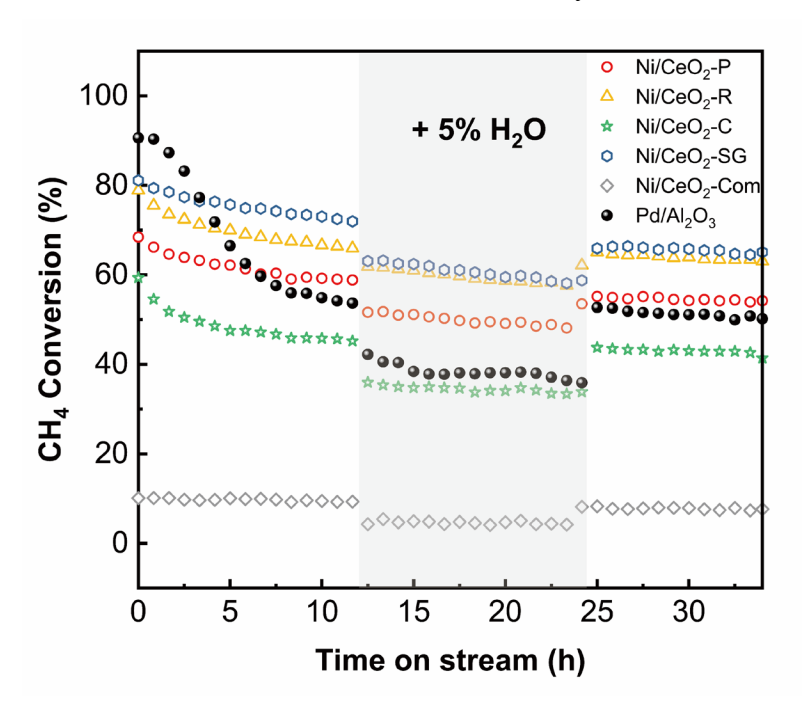


Fig. 5. Stability tests of Ni/CeO₂-P, R, C, SG, Com and 0.5 wt.% Pd/Al₂O₃ catalysts for the CH₄ oxidation reaction at 450 °C.

3.5. TEM-EDS analysis of catalysts after stability test

Fig. S4 shows the ADF-STEM images of Ni/CeO₂-R after stability test, no Ni particle was observed after reaction, suggestion that most of Ni species remain atomically disperse. Fig. S5 shows EDS elemental maps of O, Ce and Ni, their map composite, and the spectrum acquired from the AC-STEM image. The Ni map shows Ni dispersed on ceria rods with no nanoparticles shown from the field-of-view. However, after looking carefully through multiple regions of the sample, we were able to observe nanoparticles ~10 nm through EDS maps (Fig. S6). However, this occurrence of nanoparticles was so infrequent that after looking at the 10 regions of the sample, only two regions were found that contained only a handful of nanoparticles. Therefore, it can be concluded that Ni/CeO₂-R primarily contains atomically dispersed Ni with a small fraction of the Ni is present as nanoparticles.

EDS maps for Ni/CeO₂-C after stability test (Fig. S7) show predominantly NiO particles 20 - 25 nm in size as evident in the Ni map. The fraction of NiO nanoparticles is much higher in Ni/CeO₂-C than in Ni/CeO₂-R. The particle size of NiO is larger in Ni/CeO₂-C due to the lower surface area of ceria cubes compared to ceria rods, resulting in lower Ni dispersion. Fig. S8 shows ADF-STEM and corresponding ABF-STEM images of Ni/CeO₂-C. A FFT pattern was obtained from the boxed region of the particle in Fig. S8(B), and the diffraction spots were indexed showing they are consistent with the NiO phase. In addition, EDS maps were acquired to confirm this, and they are shown in Fig. S9.

The HRTEM images of Ni/CeO₂-SG after stability test are shown in Fig. S10 and Fig. S11. EDS was acquired from the field-of-view at a low magnification, and the spectrum shows Ni loading close to the nominal loading of 2 wt.% (Fig. S11), which is consistent with the ICP results (Table S1). In Fig. S10(A), EDS was acquired in regions marked with the white circles. Although the overall Ni loading is close to 2 wt.%, locally there are regions where the Ni loading is higher than 2 wt.%. Fig. S10(B) shows a higher magnification image of the boxed region in Fig. S10(A), and EDS was acquired in the region marked with the white circle with a Ni loading close to the nominal loading. Fig. S10(C) and S10(D) show the crystalline nature of the ceria nanoparticles in Ni/CeO₂-SG, but in these regions the Ni loading is much less (0.3 - 0.5 wt.%) than in Fig. S10(A) (> 2 wt.%). Although Ni loading varies locally from one region to another, on average the Ni loading in the bulk is close to 2 wt.%. Furthermore, nanoparticles were not observed by HRTEM other than the ceria crystallites (Fig. S10). Ni is present everywhere in the sample as confirmed

by EDS, and presumably, Ni is in atomically dispersed form. It has been reported previously that 10 mol% Ni can be substituted into ceria in the form of atomically dispersed species. S12 shows EDS elemental maps of O, Ce and Ni, their map composite, and the spectrum acquired from the AC-STEM image. The Ni map shows Ni dispersed on sol-gel ceria with no indication of any nanoparticles in the spent sample. Since nanoparticles were not observed by HRTEM neither, it is likely that Ni is in atomically dispersed form. In AC-STEM mode, single Ni atoms on ceria cannot be observed since nickel has a lower atomic number than cerium and does not provide the contrast expected from single Pt atoms that are easy to image. Therefore, these EDS elemental maps are the only evidence for the dispersion of Ni in Ni/CeO2-SG. Multiple regions in this sample were imaged and nanoparticles were not fund; hence, it can be concluded that the catalytic activity must be associated with atomically dispersed Ni over Ni/CeO2-SG.

4. Conclusions

Understanding the effect of nanostructure is the key for rational catalyst design and tuning the catalyst support morphologies can potentially improve the catalyst performance without change its composition. In this work, CeO₂ supports and Ni/CeO₂ catalysts with different CeO₂ morphologies (nanoparticle, rod, cube) and synthesis methods (precipitation, sol-gel) were evaluated towards the CH₄ oxidation reaction. The results showed that CeO₂-R had a greater amount of surface oxygen vacancies, an improved OSC and CH₄ oxidation activity compared to CeO₂-P and CeO₂-C. The CH₄ oxidation activity of CeO₂ support and Ni/CeO₂ catalysts improved in the same order (CeO₂-C < CeO₂-P < CeO₂-R and Ni/CeO₂-C < Ni/CeO₂-P < Ni/CeO₂-R). Increasing the CeO2 surface area by using a sol-gel synthesis method (CeO2-SG) increased the amount of surface oxygen vacancies and thus led to an improved CH₄ oxidation performance of CeO₂-SG support and Ni/CeO₂-SG catalyst compared to CeO₂-R and Ni/CeO₂-R, respectively. Interestingly, all studied Ni/CeO₂ catalysts showed an improved H₂O resistance and stability compared to conventional Pd/Al₂O₃. However, wet impregnation of Ni on CeO₂ supports with different morphologies resulted in different Ni dispersions and Ni species (atomically dispersed Ni, NiO particles), which led to challenges in comparing the TOFs of different samples. Thus, future works will focus on controlling the type of Ni species on different supports by using colloidal synthesis.

Supporting information. ICP-OES results, N₂ adsorption/desorption isotherms, light-off cycles, ADF-STEM images, EDS maps, HRTEM images (Table S1, Fig. S1-S12).

Acknowledgments:

This work was partially supported by start-up funding from the Department of Chemical and Biological Engineering, University at Buffalo (UB), The State University of New York (SUNY). A portion of this research was sponsored by the Laboratory Directed Research and Development Program of Oak Ridge National Laboratory, managed by UT-Battelle, LLC, for the U. S. Department of Energy. Dr. Eleni Kyriakidou and Junjie Chen would also like to acknowledge the Mark Diamond Research Fund of the Graduate Student Association at UB, SUNY. Financial support for the catalyst characterization via TEM was provided by the U.S. Department of Energy (DOE)/BES Catalysis Science program, grant DE-FG02-05ER15712. Additional support was provided by the DOE Energy Efficiency and Renewable Energy (EERE), Vehicle Technologies Office (DE-FOA-0002197). Acquisition of the TEM was supported by the NSF MRI grant DMR-1828731.

References:

- 1. Nie, L.; Mei, D.; Xiong, H.; Peng, B.; Ren, Z.; Hernandez, X. I. P.; DeLaRiva, A.; Wang, M.; Engelhard, M. H.; Kovarik, L., Activation of Surface Lattice Oxygen in Single-Atom Pt/CeO₂ for Low-Temperature CO Oxidation. *Science* **2017**, 358, 1419-1423.
- 2. Cargnello, M.; Jaén, J. D.; Garrido, J. H.; Bakhmutsky, K.; Montini, T.; Gámez, J. C.; Gorte, R.; Fornasiero, P., Exceptional Activity for Methane Combustion over Modular Pd@CeO₂ Subunits on Functionalized Al₂O₃. *Science* **2012**, 337, 713-717.
- 3. Senftle, T. P.; Van Duin, A. C.; Janik, M. J., Methane Activation at the Pd/CeO₂ Interface. *ACS Catal.* **2016,** 7, 327-332.
- 4. Spezzati, G.; Su, Y.; Hofmann, J. P.; Benavidez, A. D.; DeLaRiva, A. T.; McCabe, J.; Datye, A. K.; Hensen, E. J., Atomically Dispersed Pd-O Species on CeO₂ (111) as Highly Active Sites for Low-Temperature CO Oxidation. *ACS Catal.* **2017**, 7, 6887-6891.
- 5. Chen, S.; Li, S.; You, R.; Guo, Z.; Wang, F.; Li, G.; Yuan, W.; Zhu, B.; Gao, Y.; Zhang, Z., Elucidation of Active Sites for CH₄ Catalytic Oxidation over Pd/CeO₂ Via Tailoring Metal–Support Interactions. *ACS Catal.* **2021**, 11, 5666-5677.

- 6. You, R.; Zhang, X.; Luo, L.; Pan, Y.; Pan, H.; Yang, J.; Wu, L.; Zheng, X.; Jin, Y.; Huang, W., Nbo_x/CeO₂-Rods Catalysts for Oxidative Dehydrogenation of Propane: Nb-CeO₂ Interaction and Reaction Mechanism. *J Catal.* **2017**, 348, 189-199.
- 7. Rodriguez, J. A.; Liu, Z.; Lustemberg, P.; Gutierrez, R.; Carey, J.; Palomino, R.; Vorohta, M.; Grinter, D.; Ramirez, P.; Matolin, V., In Situ Investigation of Methane Dry Reforming on M-CeO₂ (111){M= Co, Ni, Cu} Surfaces: Metal-Support Interactions and the Activation of Ch Bonds at Low Temperature. *Angew. Chem. Inter. Ed.* **2017**, 56, 13041-13046.
- 8. Aranifard, S.; Ammal, S. C.; Heyden, A., On the Importance of Metal–Oxide Interface Sites for the Water–Gas Shift Reaction over Pt/CeO₂ Catalysts. *J Catal.* **2014**, 309, 314-324.
- 9. Ma, Z.; Sheng, L.; Wang, X.; Yuan, W.; Chen, S.; Xue, W.; Han, G.; Zhang, Z.; Yang, H.; Lu, Y., Oxide Catalysts with Ultrastrong Resistance to So2 Deactivation for Removing Nitric Oxide at Low Temperature. *Adv. Mater.* **2019**, 31, 1903719.
- 10. Liu, X. W.; Zhou, K. B.; Wang, L.; Wang, B. Y.; Li, Y. D., Oxygen Vacancy Clusters Promoting Reducibility and Activity of Ceria Nanorods. *J. Am. Chem. Soc.* **2009**, 131, 3140-+.
- 11. Qiao, Z. A.; Wu, Z.; Dai, S., Shape-Controlled Ceria-Based Nanostructures for Catalysis Applications. *ChemSusChem* **2013**, 6, 1821-1833.
- 12. Trovarelli, A.; Llorca, J., Ceria Catalysts at Nanoscale: How Do Crystal Shapes Shape Catalysis? *ACS Catal.* **2017**, 7, 4716-4735.
- 13. Huang, W.; Gao, Y., Morphology-Dependent Surface Chemistry and Catalysis of CeO₂ Nanocrystals. *Catal. Sci. Tech.* **2014**, 4, 3772-3784.
- 14. Wu, Z.; Li, M.; Overbury, S. H., On the Structure Dependence of CO Oxidation over CeO₂ Nanocrystals with Well-Defined Surface Planes. *J Catal.* **2012**, 285, 61-73.
- 15. Vilé, G.; Colussi, S.; Krumeich, F.; Trovarelli, A.; Pérez-Ramírez, J., Opposite Face Sensitivity of CeO₂ in Hydrogenation and Oxidation Catalysis. *Angew. Chem. Inter. Ed.* **2014,** 53, 12069-12072.
- 16. Zhang, D.; Du, X.; Shi, L.; Gao, R., Shape-Controlled Synthesis and Catalytic Application of Ceria Nanomaterials. *Dalton Trans.* **2012,** 41, 14455-14475.
- 17. Ren, C.; Yang, R.; Li, Y.; Wang, H., Modulating of Facets-Dependent Oxygen Vacancies on Ceria and Its Catalytic Oxidation Performance. *Res. Chem. Intermed.* **2019**, 45, 3019-3032.
- 18. Feng, Z.; Ren, Q.; Peng, R.; Mo, S.; Zhang, M.; Fu, M.; Chen, L.; Ye, D., Effect of CeO₂ Morphologies on Toluene Catalytic Combustion. *Catal. Today* **2019**, 332, 177-182.

- 19. Zhang, X.; You, R.; Li, D.; Cao, T.; Huang, W., Reaction Sensitivity of Ceria Morphology Effect on Ni/CeO₂ Catalysis in Propane Oxidation Reactions. *ACS Appl. Mater. Inter.* **2017**, 9, 35897-35907.
- 20. Wang, Z.; Huang, Z.; Brosnahan, J. T.; Zhang, S.; Guo, Y.; Guo, Y.; Wang, L.; Wang, Y.; Zhan, W., Ru/CeO₂ Catalyst with Optimized CeO₂ Support Morphology and Surface Facets for Propane Combustion. *Environ.Sci. Tech.* **2019**, 53, 5349-5358.
- 21. Singhania, N.; Anumol, E.; Ravishankar, N.; Madras, G., Influence of CeO₂ Morphology on the Catalytic Activity of CeO₂-Pt Hybrids for CO Oxidation. *Dalton Trans.* **2013**, 42, 15343-15354.
- 22. Ha, H.; Yoon, S.; An, K.; Kim, H. Y., Catalytic CO Oxidation over Au Nanoparticles Supported on CeO₂ Nanocrystals: Effect of the Au-CeO₂ Interface. *ACS Catal.* **2018**, 8, 11491-11501.
- 23. Farrauto, R. J., Low-Temperature Oxidation of Methane. *Science* **2012**, 337, 659-660.
- 24. Li, T.; Yao, Y.; Huang, Z.; Xie, P.; Liu, Z.; Yang, M.; Gao, J.; Zeng, K.; Brozena, A. H.; Pastel, G., Denary Oxide Nanoparticles as Highly Stable Catalysts for Methane Combustion. *Nat. Catal.* **2021**, 4, 62-70.
- 25. Chen, J.; Giewont, K.; Walker, E. A.; Lee, J.; Niu, Y.; Kyriakidou, E. A., Cobalt-Induced Pdo Formation in Low-Loading Pd/BEA Catalysts for CH₄ Oxidation. *ACS Catal.* **2021**, 11, 13066-13076.
- Zhang, X.; House, S. D.; Tang, Y.; Nguyen, L.; Li, Y.; Opalade, A. A.; Yang, J.; Sun, Z.; Tao, F., Complete Oxidation of Methane on NiO Nanoclusters Supported on CeO₂ Nanorods through Synergistic Effect. *ACS Sustain. Chem. Eng.* **2018**, 6, 6467-6477.
- 27. Chen, J.; Carlson, B. D.; Toops, T. J.; Li, Z.; Lance, M. J.; Karakalos, S. G.; Choi, J. S.; Kyriakidou, E. A., Methane Combustion over Ni/Ce_xZr_{1-x}O₂ Catalysts: Impact of Ceria/Zirconia Ratio. *ChemCatChem* **2020**, 12, 5558-5568.
- 28. Chen, J.; Buchanan, T.; Walker, E. A.; Toops, T. J.; Li, Z.; Kunal, P.; Kyriakidou, E. A., Mechanistic Understanding of Methane Combustion over Ni/CeO₂: A Combined Experimental and Theoretical Approach. *ACS Catal.* **2021,** 11, 9345-9354.
- 29. Carltonbird, M.; Eaimsumang, S.; Pongstabodee, S.; Boonyuen, S.; Smith, S. M.; Luengnaruemitchai, A., Effect of the Exposed Ceria Morphology on the Catalytic Activity of

- Gold/Ceria Catalysts for the Preferential Oxidation of Carbon Monoxide. *Chem. Eng. J.* **2018**, 344, 545-555.
- 30. Riley, C.; Canning, G.; De La Riva, A.; Zhou, S.; Peterson, E.; Boubnov, A.; Hoffman, A.; Tran, M.; Bare, S. R.; Lin, S.; Guo, H.; Datye, A., Environmentally Benign Synthesis of a Pgm-Free Catalyst for Low Temperature CO Oxidation. *Appl. Catal.*, *B-Environ.* **2020**, 264, 118547.
- 31. Scherrer, P. In *Kolloidchemie Ein Lehrbuch*, Springer: 1912; pp 387-409.
- 32. Chen, J.; Rohani, P.; Karakalos, S. G.; Lance, M. J.; Toops, T. J.; Swihart, M. T.; Kyriakidou, E. A., Boron-Hyperdoped Silicon for the Selective Oxidative Dehydrogenation of Propane to Propylene. *Chem. Commun.* **2020**, 56, 9882-9885.
- 33. Agarwal, S.; Lefferts, L.; Mojet, B. L.; Ligthart, D. M.; Hensen, E. J.; Mitchell, D. R.; Erasmus, W. J.; Anderson, B. G.; Olivier, E. J.; Neethling, J. H., Exposed Surfaces on Shape-Controlled Ceria Nanoparticles Revealed through Ac-Tem and Water-Gas Shift Reactivity. *ChemSusChem* **2013**, 6, 1898-1906.
- 34. Huang, H.; Dai, Q.; Wang, X., Morphology Effect of Ru/CeO₂ Catalysts for the Catalytic Combustion of Chlorobenzene. *Appl. Catal. B Environ.* **2014**, 158, 96-105.
- 35. Wu, Z.; Li, M.; Howe, J.; Meyer III, H. M.; Overbury, S. H., Probing Defect Sites on CeO₂ Nanocrystals with Well-Defined Surface Planes by Raman Spectroscopy and O₂ Adsorption. *Langmuir* **2010**, 26, 16595-16606.
- 36. Lyu, Y.; Jocz, J.; Xu, R.; Stavitski, E.; Sievers, C., Nickel Speciation and Methane Dry Reforming Performance of Ni/Ce_xZr_{1-x}O₂ Prepared by Different Synthesis Methods. *ACS Catal.* **2020**, 10, 11235-11252.
- 37. Huang, W.; Goodman, E. D.; Losch, P.; Cargnello, M., Deconvoluting Transient Water Effects on the Activity of Pd Methane Combustion Catalysts. *Ind. Eng. Chem. Res.* **2018**, 57, 10261-10268.
- 38. Riley, C.; De La Riva, A.; Zhou, S.; Wan, Q.; Peterson, E.; Artyushkova, K.; Farahani, M. D.; Friedrich, H. B.; Burkemper, L.; Atudorei, N.-V.; Lin, S.; Guo, H.; Datye, A., Synthesis of Nickel-Doped Ceria Catalysts for Selective Acetylene Hydrogenation. *ChemCatChem* **2019**, 11, 1526-1533.
- 39. Jones, J.; Xiong, H.; DeLaRiva, A. T.; Peterson, E. J.; Pham, H.; Challa, S. K.; Qi, G.; Oh, S.; Wiebenga, M. H.; Hernandez, X. I. P.; Wang, Y.; Datye, A. K., Thermally Stable Single-Atom Platinum-on-Ceria Catalysts Via Atom Trapping. *Science* **2016**, 353, 150.

Table of Contents

